ADVANCED MATERIALS INTERFACES Open Access
www.advmatinterfaces.de

Check for updates

Amorphous Doped Indium Tin Oxide Thin-Films by Atomic Layer Deposition.Insights into Their Structural, Electronic and Device Reliability

*M. Isabelle Büschges, Vanessa Trouillet, Ann-Christin Dippel, and Jörg J. Schneider**

Thin semiconducting films of magnesium doped indium- and tin oxide are prepared by thermal atomic layer deposition (ALD). The metal oxide films are deposited at 200 °C from the precursors trimethylindium, tetrakis (dimethylamido)tin, bis(ethylcyclopentadienyl)magnesium and water as oxidant. These thin-films are observed to be amorphous by electron microscopy and X-ray diffraction. However, they exhibited a near-range atomic order with correlation lengths of up to 10 Å, as demonstrated by high energy total scattering at grazing incidence employing synchrotron radiation. Even minor alterations in composition reveal a significant impact on the thin-film transistor (TFT) device parameters, due to magnesium's high oxygen binding capability and its ability to inhibit the formation of oxygen vacancies, resulting in a decrease of free charge carriers in the material. Stability tests indicate a device degradation after storage in ambient conditions due to water adsorption on the surface, which could be reversed by an additional annealing step which qualify the films as robust. This studie demonstrate the possibility of employing minor amounts of high band gap oxides such as MgO to manipulate and control the electric behavior of the active channel layer performance in inorganic TFT devices.

1. Introduction

Metal oxide-based thin-film transistors (TFTs) are vital components in modern electronic devices. They offer high charge carrier mobilities and high optical transparency and have been integrated into a multitude of prominent devices, including transparent and flexible displays.[1–3] Basic and applied research is presently focused on active layers comprising of In_2O_3, ZnO, SnO_2, and Ga_2O_3, particularly on ternary and quaternary combinations of these metal oxides such as In—Zn—O (IZO),[4–7] Zn—Sn—O (ZTO),[8,9] In—Zn—Sn—O (IZTO),[10,11] and In—Ga—Zn—O (IGZO).[12–15] A significant proportion of research in this field is devoted to In_2O_3, largely due to its advantageous properties, including high chemical stability and resistance to oxidation. Its thin-films exhibit noteworthy carrier mobilities, along with electrical uniformity, and high transparency to visible light (E_g = 3.7 eV).[16–18] SnO_2 represents an attractive alternative, exhibiting n-type semiconducting properties with low resistivity values and high transparency, attributed to its wide bad gap (E_g = 3.6 eV).[19] Indium tin oxide (ITO), a transparent conductive film material, has been established as the material of choice for display devices in, e.g., optoelectronics due to its unique optical and electrical properties.[20] These properties, including a relatively low resistivity and high visible transmittance, contribute to ITO's suitability for these applications.[20,21] However, ITO also exhibits an inherently high carrier density of ≈10^{20} cm^{-3}, which results in metallic-like conductivity. Consequently, it appears to be an unsuitable material for use in TFT applications.[20–22] Furthermore, polycrystalline ITO films frequently present inhomogeneous device performance over larger areas.[21] These issues can be mitigated by doping indium tin oxide with titanium (Ti-doped ITO), a material capable of inhibiting the formation of oxygen vacancies and, consequently, modulating the carrier density.[22] The enhancement of ZTO TFTs has been achieved through the incorporation of metals, including aluminum (AlZnSnO),[23] zirconium (ZrZnSnO),[24] gallium (GaZnSnO),[25] and magnesium (MgZnSnO).[18] Due to their relatively low electronegativity, the tendency to form strong M—O bonds increases, thereby

M. I. Büschges, J. J. Schneider
Fachbereich Chemie
Eduard-Zintl-Institut
Technische Universität Darmstadt
Peter-Grünberg-Straße 12, 64287 Darmstadt, Germany
E-mail: joerg.schneider@tu-darmstadt.de
V. Trouillet
Institute for Applied Materials (IAM-ESS) and Karlsruhe Nano Micro Facility (KNMFi)
Karlsruhe Institute of Technology (KIT)
Hermann-von-Helmholtz-Platz 1, 76344 Eggenstein-Leopoldshafen, Germany
A.-C. Dippel
Deutsches Elektronen-Synchrotron DESY
Notkestraße 85, 22607 Hamburg, Germany

The ORCID identification number(s) for the author(s) of this article can be found under https://doi.org/10.1002/admi.202400758

© 2024 The Author(s). Advanced Materials Interfaces published by Wiley-VCH GmbH. This is an open access article under the terms of the Creative Commons Attribution License, which permits use, distribution and reproduction in any medium, provided the original work is properly cited.

DOI: 10.1002/admi.202400758

reducing the amount of oxygen vacancies. As oxygen vacancies represent the primary source of charge carriers in amorphous oxide semiconductors (AOS), these metals serve as effective charge carrier suppressors, as evidenced by previous research.[16,18] The efficacy of incorporating metal ions to suppress charge carriers has been demonstrated in a multitude of systems[26] including MgZnO,[27] MgInO,[28–30] HfInZnO,[31,32] Al-doped ITO,[33] and ZrInZnO.[34,35] The fabrication of such multi-component thin-films is made possible by employing a method such as atomic layer deposition (ALD). With ALD, excellent conformality and composition- and thickness control on the atomic scale can be achieved even at low growth temperatures (<350 °C).[36,37] ALD is a highly developed thin-film deposition technique, based on the sequential exposure of precursors and co-reactants to the surface of a solid substrate. The reactions are self-limiting on the surface, allowing a layer-by-layer growth.[36–39] The ALD approach of employing supercycles allows the deposition of homogeneous multi-component and multilayered thin-films with control of the cation distribution by adjusting the cycle ratios of the individual binary materials.[37,39] In such a multi-component system, each metal cation can contribute to different functions in the resulting film, such as main charge carrier, charge carrier suppressor or structure stabilizer.[39] By fabricating amorphous IGZO by ALD using such a supercycle approach, mobilities (μ) of up to 74 $cm^2\ V^{-1}\ s^{-1}$ have been achieved with a threshold voltage (V_{th}) of −1.3 V and a subthreshold swing (SS) of 0.26 V dec^{-1}.[40,41] With its advantages of depositing oxides over large areas with good uniformity and compositional control, ALD has become the most reliable deposition technique for semiconductor processes,[36,39,42] and has therefore even attracted interest in other application areas such as energy storage,[43] photovoltaics,[44] and catalysis.[45] In this study, we report, for the first time, on the doping of ITO thin-films with the large band gap oxide MgO using ALD as fabrication method. Our approach of doping ITO with magnesium oxide is based on the specific properties of the material and findings from published literature,[26–30] which substantiate the modulation of the charge carrier concentration through the introduction of an element with a high binding energy. Moreover, the identified shortcomings of ITO can be mitigated. Magnesium oxide was selected as the doping material due to its cost-effectiveness, availability, and precedent for use in similar systems. The doping of ITO with magnesium oxide was investigated in our system, as this material combination proved to be promising for the intended purposes. The objective of this study is to examine the subtle impact of MgO on the semiconducting characteristics of ITO films. This work demonstrates how MgO, as an oxide with a high oxygen binding energy, can be employed as a controllable charge carrier suppressor for these films. The ultrathin films obtained in this study were found to be amorphous, as determined by high-resolution transmission electron microscopy (HRTEM). Of particular interest was the revelation of near-atomic scale ordering through grazing incidence X-ray diffraction (GIXRD) under synchrotron radiation.

The influence of magnesium oxide on the TFT performance parameters under ambient dry and wet conditions was further investigated by incorporating the thin-films into TFT devices, as was the stability of the thin-films under illumination with different wavelength.

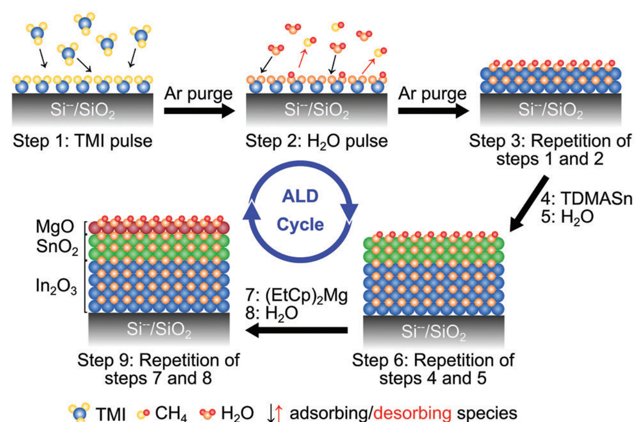

Figure 1. Schematic of the ALD process for the heterostack preparation of MITO. For the deposition of indium oxide from TMI and H_2O the steps are shown in detail (step 1–3). In step 1 the TMI molecules react with OH-groups on the surface of the substrate; by purging with argon the residual precursor molecules are flushed from the reaction chamber. In step 2 H_2O is introduced, reacting with the newly formed surface groups to produce new OH-groups and CH_4 as by-product. With a subsequent argon purge unreacted molecules and by-products are removed from the chamber. By repetition of steps 1–2 the thickness of the indium oxide layer can be modulated (step 3). For depositing tin oxide from TDMASn (steps 4–6) and magnesium oxide from $(EtCp)_2Mg$ (steps 7–9), the process is performed as described above. Thin-films with a composition of $In_xO_y/SnO_x/MgO$ 26:15:1 (MITO 1), 26:15:2 (MITO 2), and 26:15:3 (MITO 3) are deposited in eight supercycles.

2. Results and Discussion

Three heterostacks consisting of indium oxide, tin oxide, and magnesium oxide are fabricated via ALD by depositing the single oxides with a fixed number of cycles for indium- and tin oxide, while the number of magnesium oxide cycles was varied between one and three in order to study the influence of an insulating material on the morphology of the thin-films and in particular on the semiconducting properties of the MgInSnO (Magnesium-Indium-Tin Oxide; MITO) heterostructure stack when integrated into a thin-film transistor device. In **Figure 1** schematic of the deposition process for one supercycle is depicted. In the first step metal precursor molecules, here trimethylindium (TMI), react with surface OH-groups of the substrate (step 1), thereby In—O bonds are formed. The following purge step with inert gas (argon) removes excess metal precursor and gaseous reaction by-products. Subsequently the oxidizing agent (H_2O) is introduced into the reaction chamber (step 2). Remaining methyl groups of the TMI react to CH_4 and new OH-groups are formed on the surface. After purging the chamber with argon, the sequence is repeated (step 3) until the desired film thickness of indium oxide is obtained. Tin oxide and magnesium oxide are deposited from tetrakis(dimethylamido)tin (TDMASn, steps 4–6) and bis(ethylcyclopentadienyl) magnesium ($(EtCp)_2Mg$, steps 7–9), respectively, and oxidized with water, as described for indium oxide above. By performing steps 1–9 one ALD cycle is completed, which is repeated to achieve the desired overall film thickness. This process enables the deposition of a heterostack with a defined composition, as

© 2024 The Author(s). Advanced Materials Interfaces published by Wiley-VCH GmbH

21967350, 0, Downloaded from https://onlinelibrary.wiley.com/doi/10.1002/admi.202400758 by Karlsruher Institut F., Wiley Online Library on [02/12/2024]. See the Terms and Conditions (https://onlinelibrary.wiley.com/terms-and-conditions) on Wiley Online Library for rules of use; OA articles are governed by the applicable Creative Commons License

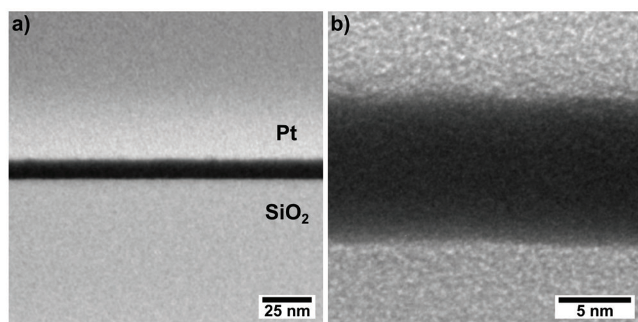

Figure 2. Cross-sectional HRTEM bright field image of the heterostack MITO 2 with the composition $In_xO_y/SnO_x/MgO$ 26:15:2. The conformal layer thickness over a large area can be observed a). The amorphous nature of the heterostack at a higher magnification is shown b).

well as control over the thickness of the individual oxides on an atomic level. In the experimental section the exact parameters for the deposition of each precursor is given. Thin-films with a composition of 26 cycles indium oxide, 15 cycles tin oxide, and one to three cycles of magnesium oxide are deposited in eight complete supercycles (see caption of Figure 1 for denotation of individual samples).

The heterostructure composition is investigated using high resolution transmission microscopy (HRTEM), high energy total X-ray scattering in gracing incidence (GIXRD), X-ray photoelectron spectroscopy (XPS), and UV–vis spectroscopy. To assess the semiconducting properties of the heterostacks with different compositions, they were integrated into thin-film transistor devices.

High resolution transmission electron microscopy (HRTEM) is performed on a focused ion beam (FIB) prepared cross-section of the sample MITO 2 to investigate the homogeneity and morphology of the thin-film (**Figure 2**). The HRTEM of the heterostack MITO 2 reveals a uniform film thickness of ≈10 nm over an extensive area with a high degree of homogeneity, revealing the conformity during the deposition process. The thin-film appears to be amorphous over the whole stack, without a noticeable layered architecture as seen in other ALD deposited thin-films, employing aluminum oxide instead of magnesium oxide in combination with indium oxide and tin oxide.[33] The amorphous nature of magnesium oxide films has already been reported for ALD deposited MgO at temperatures of 200 °C,[46] while crystallinity was only observed at temperatures above 500 °C.[47]

To gain further insight into the structure of the heterostack thin-films, grazing incidence X-ray total scattering (GI-XTS) measurements using synchrotron radiation are conducted. Pair distribution function (PDF) analysis is used to study the atomic short-range order of the samples, as well as to elucidate the influence of the magnesium oxide incorporation on the thin-films structure. In **Figure 3** the obtained PDF data for the ALD prepared samples MITO and ITO (Figure 3a), together with references for pure In_2O_3[48] and ITO of different compositions[49–51] (Figure 3b,c) are shown. The PDFs of the two ALD samples MITO and ITO show a very disordered structure with correlation lengths of ≈10 Å (Figure 3a), with three rather distinct peaks at ≈2.1, 3.4, and 3.8 Å and broader signals at interatomic distances greater than 5 Å. As the PDFs for both samples are very similar, regardless of their composition and thickness, they are not discussed separately.

The values of the three peaks for the ALD samples can be correlated with interatomic distances found in the crystalline reference structures, which show similar peaks in the range of 1.75–4.75 Å.[48–51] In the crystalline ITO-references, $In_{1.88}Sn_{0.12}O_3$ (space group $Ia\bar{3}$, cubic), $In_4Sn_3O_{12}$ (space group $R\bar{3}$, trigonal), and $Sn(Sn_2In_4)O_{12}$ (space group $R\bar{3}$, trigonal), a distance of 2.1 Å correlates with nearest neighbor metal-oxygen bonds (In/Sn—O). Metal-metal next-nearest neighbor distances exhibit values of ≈3.4 Å, while mixed longer distances show values of ≈3.8 Å. Cubic In_2O_3 (space group $I213$)[48] shows peaks at 2.3, 3.4, and 3.8 Å, correlated to In—O bonds and metal-metal distances, respectively. The comparison of the samples' PDFs with the reference In_2O_3 and the three crystalline ITO-compositions (Figure 3c) shows that the peak at 2.1 Å corresponds to nearest neighbor metal-oxygen distances (In/Sn—O) in the ITO-references, while the peaks at 3.4 and 3.8 Å fit with values found for metal-metal distances in In_2O_3 and ITO with a high indium content ($In_{1.88}Sn_{0.12}O_3$). Therefore, it can be concluded that both ALD samples (MITO and ITO) exhibit a short-range order resembling those found in the reference

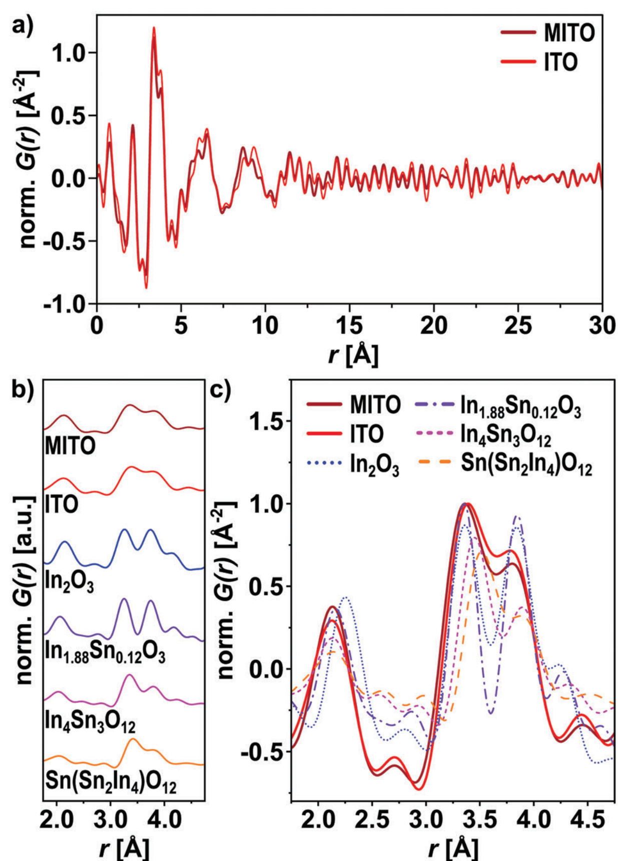

Figure 3. a) Normalized PDFs obtained for the ALD samples MITO and ITO shown over the full r range (0-30 Å). In b) and c) a comparison of the samples and calculated PDFs for reference In_2O_3 (blue) and indium tin oxide (violet, magenta, orange) of different compositions, b) shown in a stacked plot and c) as overlay for a better comparison of the interatomic distances of the ALD samples and references. For clarity, only the low-r region from 1.75–4.75 Å is shown. A graph of the full distance range can be found in Figure S1 (Supporting Information).

© 2024 The Author(s). Advanced Materials Interfaces published by Wiley-VCH GmbH

21967350, 0, Downloaded from https://onlinelibrary.wiley.com/doi/10.1002/admi.202400758 by Karlsruher Institut F., Wiley Online Library on [02/12/2024]. See the Terms and Conditions (https://onlinelibrary.wiley.com/terms-and-conditions) on Wiley Online Library for rules of use; OA articles are governed by the applicable Creative Commons License

21967350, 0, Downloaded from https://onlinelibrary.wiley.com/doi/10.1002/admi.202400758 by Karlsruher Institut F., Wiley Online Library on [02/12/2024]. See the Terms and Conditions (https://onlinelibrary.wiley.com/terms-and-conditions) on Wiley Online Library for rules of use; OA articles are governed by the applicable Creative Commons License

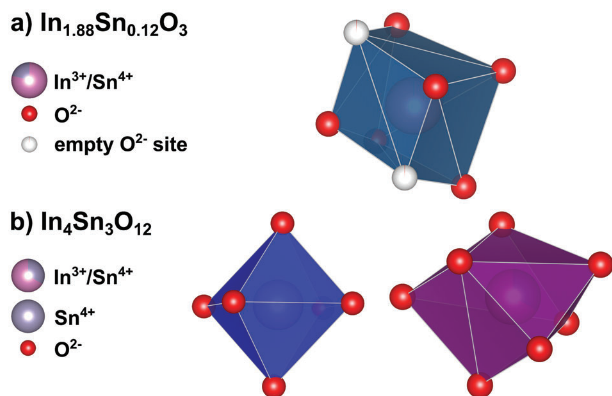

Figure 4. Coordination polyhedra as found for In^{3+} and Sn^{4+} ions in $In_{1.88}Sn_{0.12}O_3$[49] and b) $In_4Sn_3O_{12}$.[50] Different colors indicate different polyhedral geometries.

compounds In_2O_3 and In-rich ITO.[48,49] However, there is no clear difference in the structural parameters concerning the inclusion of magnesium oxide. Either, this might simply be related to its low content in the MITO thin-film (cycle ratio Mg/(In+Sn) = 0.049), or the incorporated magnesium oxide could inhibit the crystallization of the otherwise crystalline ITO. For both speculations, further structural studies are necessary (PDFs of all reference phases, including the pure metal oxides SnO_2[52] and MgO,[53] can be found in Figure S1, Supporting Information). As the metal-oxygen and metal-metal distances found in the PDFs of the ALD samples do not show a considerable effect of Mg incorporation (see Figure 3b,c) and correlate well with those found for the crystalline references of In-rich ITO phases,[49,50] it can be suggested that the nearest neighbor polyhedral coordination geometries of the metal cations in the ALD samples are similar to the crystalline ITO phases $In_{1.88}Sn_{0.12}O_3$[49] and $In_4Sn_3O_{12}$[50] (**Figure 4**). In the former $In_{1.88}Sn_{0.12}O_3$ (Figure 4a) the metal cations (In^{3+}/Sn^{4+}) are coordinated by six oxygen anions and two empty anion sites in a cube like geometry.[49] In the crystal structure of $In_4Sn_3O_{12}$[50] (Figure 4b) the metal cations show two different coordination geometries. Sn^{4+} cationic sites are surrounded by six oxygen anions in a trigonally compressed octahedron (blue), while In^{3+}/Sn^{4+} cationic sites are coordinated by seven oxygen anions in a geometry described as a highly distorted cube with one missing corner (purple).[49,50]

The heterostack compositions MITO 1-3 with varying magnesium oxide content were studied by X-ray photoelectron spectroscopy (XPS). The O 1*s* core level (**Figure 5a**) is deconvoluted into three peaks, allocated to different oxygen species present within the thin-films. The peak at lower binding energies (BE) of 530.0 eV can be assigned to fully coordinated oxygen species (M—O),[5,6] related to the metal oxides indium oxide, tin oxide, and magnesium oxide. The signal at a higher BE of 531.8 eV can mainly be attributed to metal hydroxide species, M—OH, typically present on the surface of the sample.[6,54,55] However, weak contributions from —C═O (carbonyl species) and/or $MgCO_3$,[56] may appear in the same BE region. This is further supported by the corresponding peaks observed in the C 1*s* core level (Figure 5b, described later). In addition, the third peak of the deconvolution at 533.2 eV can be assigned to —C—O fragments, probably originating from minor residues of the precursor $(EtCp_2)Mg$.[57,58] It should be mentioned that often O 1*s* peak assignments in the BE range of 531–532 eV are attributed to lattice oxygen atoms in close proximity to "oxygen vacancies".[59–62] However, this attribution can neither be straightforward nor fully justified especially as such vacancies often do not modify the coordination number of the vaccancies' neighbor oxygen atoms in the oxide.[63] Furthermore, the presence of surface species in the similar BE range is often ignored and/or the full width at half maximum (FWHM) are set to smaller values than they should be. With respect to our study no clear-cut spectroscopic evidence justifies the consideration of further species in this range of BE. In addition, particular attention has been paid to the FWHM for each component. They amount to the reasonable and well-known values of 1.5 eV for lattice oxygen in an oxide and 1.9 eV for hydroxide, carbonate or other carbon species.

With an increasing magnesium oxide content, the MITO samples' amount of fully oxidized M—O species decreases from 28.4 at% to 20.7 at%, while the contribution from the peak at 531.8 eV (M—OH) increases from 18.6 at% to 23.9 at%. Considering the relatively small —C═O content, as detected in the C 1*s* spectrum, increasing from 3.1 at% up to 5.5 at%,

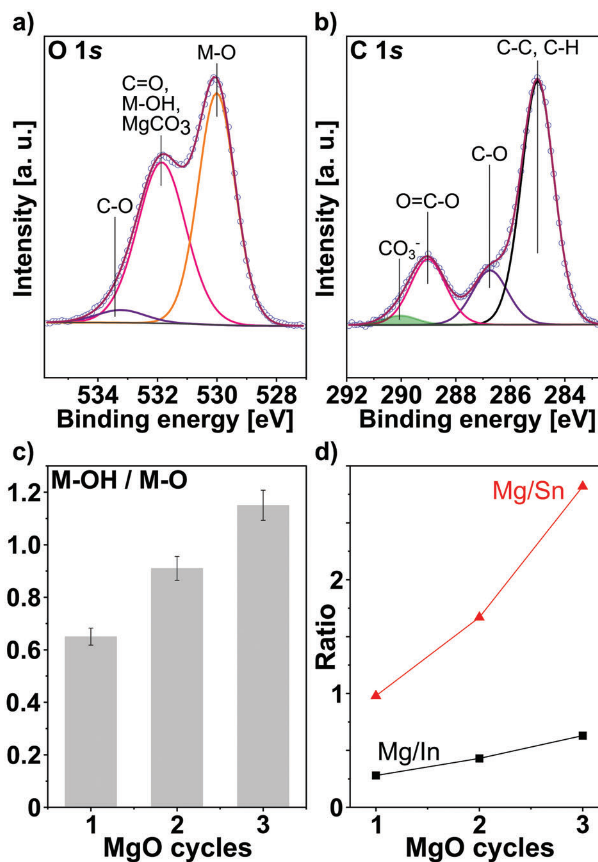

Figure 5. a) O 1*s* and b) C 1*s* XPS core level spectra of the heterostructure MITO 2. All spectra are referenced to the C 1*s* peak at 285.0 eV. In c) the ratio of M—OH (531.8 eV) to M—O (530.0 eV) is depicted, while d) represents the ratios of Mg/Sn (red) and Mg/In (black) calculated from at% of the core level spectra In 3*d*, Sn 3*d*, and Mg 1*s* for the three thin-films MITO 1-3, deposited with one, two, and three cycles of magnesium oxide.

© 2024 The Author(s). Advanced Materials Interfaces published by Wiley-VCH GmbH

this latter O 1*s* peak is essentially correlated to M—OH species. Therefore, the increase of M—OH contributions along the MITO 1-3 series can be followed by the ratio M—OH (531.8 eV) versus M—O (530.0 eV) (see Figure 5c). This increased amount of hydroxide species generated in the thin-films can be explained by an ongoing hydroxylation through the oxidant H_2O of already deposited magnesium oxide in subsequent ALD cycles. This is supported by reports of Santamaria et al., who confirmed the formation of an increasingly thicker hydroxide layer by XPS, when exposing a MgO film to an aqueous solution for a longer period of time.[64] The C 1*s* core level is deconvoluted into four peaks, located at 285.0, 286.7, 289.1, and 290.0 eV. The main peak at 285.0 eV can be associated with —C—C and —C—H groups in the form of hydrocarbon contaminations,[65,66] while the peak at 286.7 eV can be ascribed to —C—O groups originating from $(EtCp)_2Mg$ precursor residues.[58] Additionally, the peaks at 289.1 and 290.0 eV are attributed to carboxylic groups[65] and to a very minor extent (0.5 at%) to carbonate, $MgCO_3$, respectively[66,67] (all data can be found in Table S2, Supporting Information). In Figure 5d ratios for Mg/Sn and Mg/In based on the at% of the core level spectra of In 3*d*, Sn 3*d*, and Mg 1*s* for the three thin-films MITO 1-3, are given. Both ratios (Mg/Sn and Mg/In) follow the same trend: with an increasing number of magnesium oxide cycles, the values of the ratios increase, confirming that the composition set during the deposition process is also obtained in the deposited heterostructures.

The core level spectra for tin oxide, indium oxide, and magnesium oxide, as well as the valence band (VB) region and the In MNN-Auger line are shown in Figure S2a–e (Supporting Information). The Sn 3*d* doublet with Sn $3d_{5/2}$ at 486.5 eV, together with the valence band pattern with a maximum at 4.5 eV reveal the presence of Sn(IV) and are in agreement with previously reported values (see Figure S2a,d, Supporting Information).[68,69] The VB spectrum of MITO has a band width of nearly 9 eV and shows no change due to Mg doping when compared to SnO_2 deposited by chemical vapor deposition.[69] In 3*d* with In $3d_{5/2}$ at 444.5 eV (see Figure S2b, Supporting Information) and In MNN Auger (see Figure S2e, Supporting Information) prove the presence of In_2O_3.[70] The Mg 1*s* core level peak is located at 1304.0 eV (see Figure S2c, Supporting Information) and situated between the binding energy of both pure MgO and $Mg(OH)_2$ (1303.2 eV) and $MgCO_3$ (1304.6 eV).[71] Interestingly, the BE value does not change with increasing magnesium oxide incorporation (heterostacks MITO 1-3), meaning the carbonate content remains low and stable over the deposition process. Thus, the majority of Mg(II) species in the thin-films are present in the form of oxide and hydroxide. Furthermore, UV-vis spectroscopy was employed to assess the optical properties of the heterostacks MITO 1-3. All thin-films show a high optical transparency of > 95% in the visible region (**Figure 6**a). To determine the optical band gaps of the heterostacks Tauc plots were generated from the transmission data, shown in Figure 6b. Tauc plots were calculated with respect to the individual film thicknesses of the three samples.[72]

The Tauc plots exhibit different curve progressions for the three thin-films investigated, showing a strong influence of only small amounts of magnesium oxide on the optical properties. Nevertheless, the difference becomes less noticeable in the values determined for the optical band gaps by applying a linear

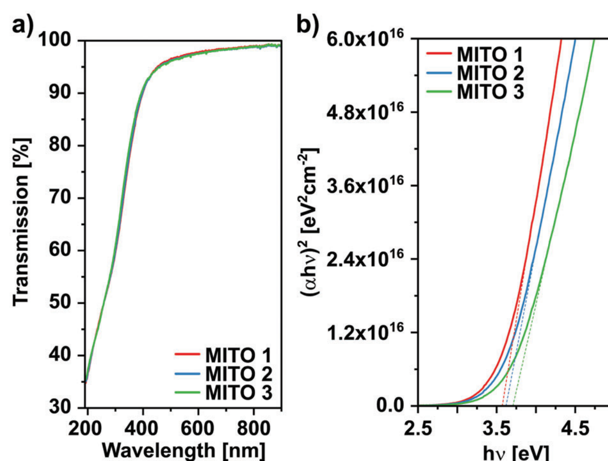

Figure 6. Transmission spectra a) and Tauc plots b) of the three investigated heterostructures MITO 1 (red), MITO 2 (blue), and MITO 3 (green).

fit. The band gap widens with an increasing amount of magnesium oxide in the thin-films from 3.57 eV for MITO 1 to 3.71 eV for MITO 3 (**Table 1**). With MgO as a material exhibiting a larger band gap (≈7.8 eV)[73–75] than In_2O_3 (3.6–3.75 eV)[76,77] and SnO_2 (3.6 eV),[19] this widening of the optical band gap is expected when increasing the amount of magnesium oxide in the MITO thin-films. A widening of the band gap through Mg-doping has also been reported for aluminum zinc oxide (AZO) films.[78]

2.1. Studies on the Semiconducting Properties of MITO Thin-Films

To assess the semiconducting properties of the three indium/tin/magnesium oxide heterostructures and to study the specific influence of the magnesium oxide doping, the thin-films were integrated into TFT devices with a bottom-gate-bottom-contact geometry. After the deposition of the thin-films and post-deposition annealing at 350 °C, the electrical characterization of the obtained TFT devices was performed by means of current-voltage (*I*–*V*) measurements. From the transfer characteristics the significant TFT performance parameters such as the saturation mobility (μ_{sat}), on-voltage (V_{on}), threshold-voltage (V_{th}), current on/off ratio (I_{on}/I_{off}), and subthreshold swing (*SS*) were extracted. The collective transfer characteristics, as well as individual output curves are shown in **Figure 7**, while the corresponding values are summarized in **Table 2**.

From the transfer characteristics it is noticeable that the amount of magnesium oxide in the heterostructure stack exerts

Table 1. Calculated band gaps obtained from the corresponding Tauc plots and respective film thicknesses of the thin-films with different magnesium oxide content MITO 1-3.

Composition In:Sn:MgO	Band gap [eV]	Thickness [nm]
26:15:1 MITO 1	3.57	9.55
26:15:2 MITO 2	3.62	10.65
26:15:3 MITO 3	3.71	12.49

© 2024 The Author(s). Advanced Materials Interfaces published by Wiley-VCH GmbH

21967350, 0, Downloaded from https://onlinelibrary.wiley.com/doi/10.1002/admi.202400758 by Karlsruher Institut F., Wiley Online Library on [02/12/2024]. See the Terms and Conditions (https://onlinelibrary.wiley.com/terms-and-conditions) on Wiley Online Library for rules of use; OA articles are governed by the applicable Creative Commons License

21967350, 0, Downloaded from https://onlinelibrary.wiley.com/doi/10.1002/admi.202400758 by Karlsruher Institut F., Wiley Online Library on [02/12/2024]. See the Terms and Conditions (https://onlinelibrary.wiley.com/terms-and-conditions) on Wiley Online Library for rules of use; OA articles are governed by the applicable Creative Commons License

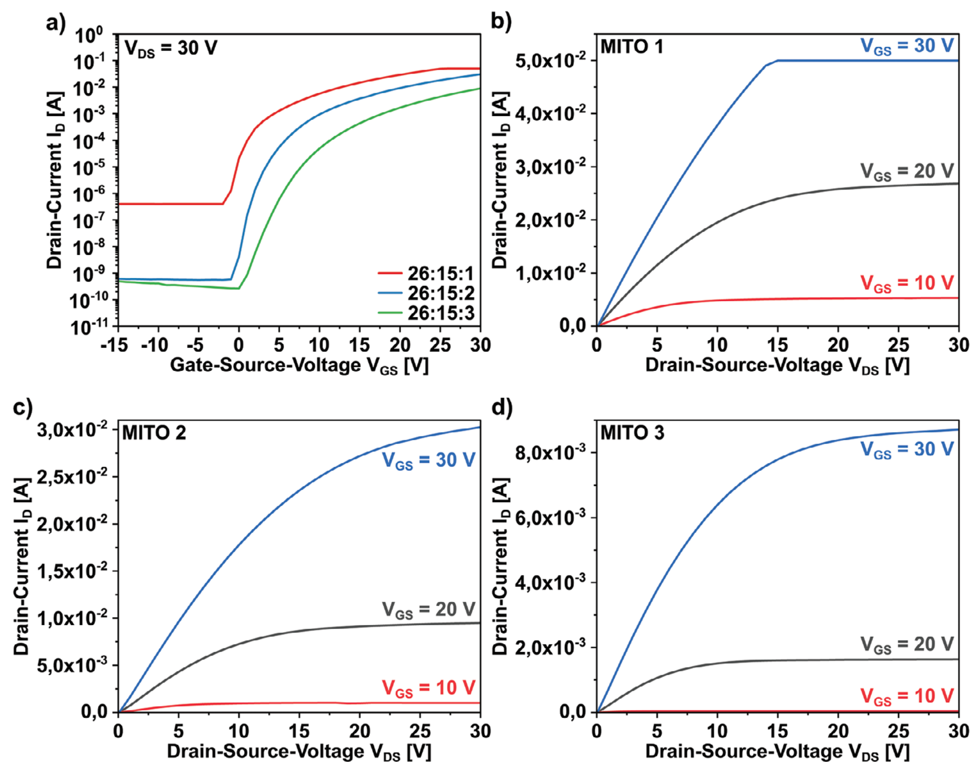

Figure 7. a) Collective transfer characteristics of the TFT devices incorporating the heterostructures with one (red), two (blue), and three (green) cycles of deposited magnesium oxide MITO 1-3, and the corresponding output characteristics of b) MITO 1, c) MITO 2, and d) MITO 3. In b), the measuring equipment reached its compliance limit of 50 mA at V_{GS} = 30 V.

an apparent influence on the off-current (I_{off}), especially when increasing the number of magnesium oxide cycles from one to two, while the increase from two to three does not show a similar drop of I_{off}. At the same time, the on-current (I_{on}) decreases to a smaller extent with an increasing amount of magnesium oxide in the stack. This is illustrated in the values for I_{on}/I_{off} starting at $1.2{\cdot}10^5$ for MITO 1, increasing to $5.3{\cdot}10^7$ for MITO 2 and slightly decreasing for MITO 3 to $3.4{\cdot}10^7$ (Figure 7a). The decrease in conductivity with increasing amounts of magnesium oxide is also apparent from the individual output characteristics (Figure 7b-d). Accompanying the decrease of I_{off} is a significant decline in the mobility values, starting at 10.64 cm^2 V^{-1} s^{-1} for MITO 1 and dropping to 3.06 cm^2 V^{-1} s^{-1} for MITO 3. These similar trends are expected when increasing the amount of the insulating component in the thin-films, as magnesium oxide, with its high resistivity in the range of 10^{11} Ω cm,[79] decreases the amount of free electrons in the semiconducting MITO film and also lowers the ability of the electrons to move, thus decreases the mobility. The TFT incorporating two cycles of magnesium oxide (MITO 2) shows the overall best performance of the investigated compositions with μ_{sat} = 6.45 cm^2 V^{-1} s^{-1}, V_{th} = 7.2 V, I_{on}/I_{off} = $5.3{\cdot}10^7$, and SS = 644 mV dec^{-1}. While a lower amount of magnesium oxide (MITO 1) leads to a significantly higher mobility and a lowered threshold voltage, the current on/off ratio and the subthreshold swing deteriorate; with a higher number of magnesium oxide cycles (MITO 3) a sufficient I_{on}/I_{off} is still reached but at the expense of a significantly lower electron mobility, as well as the subthreshold swing. The obtained values for MITO fall within the range of values reported in the literature for heterostack InZnO TFTs fabricated via ALD[6] with μ = 6.5 cm^2 V^{-1} s^{-1}, V_{th} = 8.9 V, I_{on}/I_{off} = $4.6{\cdot}10^7$, and SS = 0.7 V dec^{-1} and also for MgInO TFTs fabricated via spin-coating[28] with μ = 13.77 cm^2 V^{-1} s^{-1}, V_{th} = 2.84 V, I_{on}/I_{off} = $2.36{\cdot}10^7$, and SS = 0.85 V dec^{-1}. With respect to our earlier studies on aluminum oxide doped ITO thin-films (ITAO),[33] employing the same ALD process and TFT fabrication procedures, it is apparent that

Table 2. TFT performance parameters and corresponding standard deviations of the heterostructure TFT devices of the semiconducting MITO thin-films.

Composition In:Sn:MgO	Mobility, μ_{sat} [cm^2 V^{-1} s^{-1}]	On-voltage, V_{on} [V]	Threshold voltage, V_{th} [V]	Current on/off ratio, I_{on}/I_{off}	Subthreshold swing, SS [mV dec^{-1}]
26:15:1 MITO 1	10.64 ± 0.18	−2.0 ± 0.2	2.8 ± 0.2	1.2 (±0.27)·10^5	816 ± 27
26:15:2 MITO 2	6.45 ± 0.14	−1.0 ± 0.2	7.2 ± 0.3	5.3 (±0.30)·10^7	644 ± 33
26:15:3 MITO 3	3.06 ± 0.04	0.0 ± 0.1	12.4 ± 0.1	3.4 (±0.48)·10^7	1211 ± 11

 © 2024 The Author(s). Advanced Materials Interfaces published by Wiley-VCH GmbH

aluminum exerts a stronger influence on the TFT performance parameters than magnesium. This is noticeable in the lower mobility values of 2.28 and 6.45 $cm^2 V^{-1} s^{-1}$ for ITAO and MITO, respectively. With its distinctly higher bond dissociation energy (Al—O 501.9 kJ mol^{-1}),[80,81] the incorporated aluminum oxide can suppress oxygen vacancy formation more efficiently than magnesium oxide (Mg—O 358.2 kJ mol^{-1}),[80,81] thus leading to a lowered density of free charge carriers, influencing the electrical characteristics of the transistor to a significant extent.[25] Hall measurements in van der Pauw geometry were conducted to obtain the charge carrier densities of the three heterostacks. With the least amount of magnesium oxide, the MITO 1 thin-film exhibits the highest Hall carrier density with $5.9 \cdot 10^{19}$ cm^{-3}, while the MITO 3 film shows the lowest value with a measured carrier density of $1.1 \cdot 10^{19}$ cm^{-3}. The MITO 2 heterostack gives an intermediate value of $2.2 \cdot 10^{19}$ cm^{-3}. These values for the carrier densities follow the same trend as the mobility values obtained from the IV-measurements (Table 2), solidifying the hypothesis, that an increase of magnesium oxide decreases the number of free charge carriers in the heterostack. Furthermore, the obtained values correspond to values reported in literature with 3–$5 \cdot 10^{19}$ cm^{-3} for P-doped ZnMgO[82] and are in the upper range of 10^{16}–10^{20} cm^{-3} determined for different types of IGZO.[83] The values for the charge carrier densities found for MITO are also in accord with the trends in the performance parameters when comparing MITO with ITAO,[33] as the carrier density for ITAO is lower, owing to the significantly higher bond dissociation energy of Al—O compared to Mg—O.

The carrier transport in semiconducting materials can mainly be described by two different mechanisms: trap-limited conduction (TLC) and percolation conduction (PC). When the Fermi-Level (E_F) is located below the conduction band minimum (CBM), the charge carrier transport is primarily controlled by multiple trapping and releasing events of carriers in localized tail states, viz. TLC is the dominant transport mechanism.[84] Percolation conduction becomes dominant when E_F moves above the CBM and thereby fills tail states.[84] At this point only a distribution of potential barriers within the conduction band (CB) limits the mobility of the charge carriers.[85] The electrons move around those barriers, taking the path of least resistance.[84] To gain inside into the carrier transport mechanism of the fabricated semiconducting heterostructures MITO 1-3, the field-effect mobility (μ_{FE}) is plotted logarithmically against the gate-source voltage and a power law fit is applied (**Figure 8**).

$$\mu_{FE} = K\left(V_{GS} - V_{th,P}\right)^{\gamma} \quad (1)$$

with K as prefactor and V_{GS}, V_{th}, and V_P denoting the gate-source, threshold, and percolation voltages, respectively. The exponent γ is obtained and is correlated to the prevailing conduction mechanism. TLC is dominant if γ reaches a value of 0.7, while a value of 0.1 indicates a PC dominated mechanism.[7,84] The obtained values for γ along with the corresponding mobilities and conduction mechanisms are summarized in **Table 3**.

As indicated by the values for γ, the carrier transport mechanism changes from clearly PC to TLC dominated with an increasing amount of magnesium oxide in the heterostructure stack. With its smaller band gap of 3.57 eV and higher conductivity, compared to MITO 2 and MITO 3, the Fermi-level in the heterostack with one cycle magnesium oxide, MITO 1, appears to be positioned above the CBM, showing a clear distinction to the other two thin-films, exhibiting a PC dominated conduction mechanism. By increasing the amount of magnesium oxide, the band gap widens to 3.71 eV (MITO 3) and the conductivity diminishes, therefore E_F moves to a position below the CBM enabling tail states to act as electron traps.[84] Another reason for the clear shift from PC to TLC in the MITO thin-films when the Mg content is steadily increased could be found in the increase in weakly bonded oxygen which leads to the formation of trap states, as it is reported for amorphous Ga_2O_x films.[86] This data shows the strong influence of only small amounts of a material with a strong M—O bond on the carrier concentration and therefore on the device performance, as has been reported for Ga_2O_3,[40,41,87] here at the advantage of a low cost and abundant material in the form of magnesium oxide. As apparent from the XPS data, the amount of fully coordinated oxygen species (M—O) decreases with increasing numbers of deposited magnesium oxide cycles, while the amount of hydroxide species (M—OH) increases simultaneously, which is in accord with our assumptions. Since the temperature dependency of the mobility is a further indication and can substantiate the afore mentioned studies to determine the γ value for the prevailing transport mechanism,[84] variable low temperature measurements of the transistor characteristics were conducted. **Figure 9**

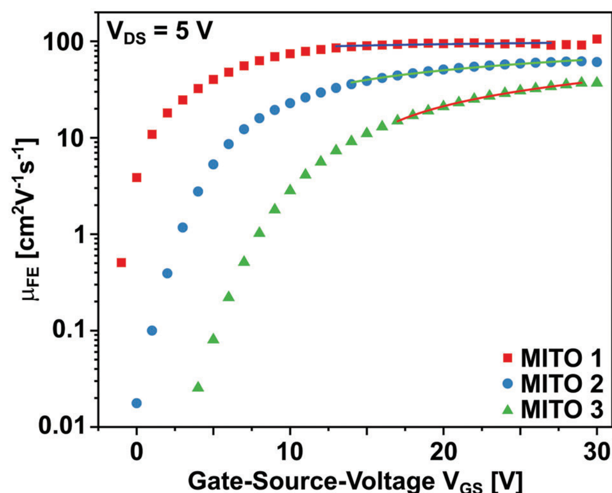

Figure 8. Dependency of the field-effect mobility (μ_{FE}) on the gate-source voltage (V_{GS}), plotted logarithmically, with the applied power law fit to obtain values for γ.

Table 3. Values for the exponent γ and mobility μ_{FE} with their corresponding standard deviations and the prevalent conduction mechanism for the three heterostructures MITO 1-3.

Composition In:Sn:MgO	γ	Mobility μ_{FE} [$cm^2 V^{-1} s^{-1}$]	Conduction mechanism
26:15:1 MITO 1	0.09 ± 0.03	10.64 ± 0.18	PC
26:15:2 MITO 2	0.46 ± 0.02	6.45 ± 0.14	PC/TLC
26:15:3 MITO 3	0.72 ± 0.01	3.06 ± 0.04	TLC

© 2024 The Author(s). Advanced Materials Interfaces published by Wiley-VCH GmbH

21967350, 0, Downloaded from https://onlinelibrary.wiley.com/doi/10.1002/admi.202400758 by Karlsruher Institut F., Wiley Online Library on [02/12/2024]. See the Terms and Conditions (https://onlinelibrary.wiley.com/terms-and-conditions) on Wiley Online Library for rules of use; OA articles are governed by the applicable Creative Commons License

21967350, 0, Downloaded from https://onlinelibrary.wiley.com/doi/10.1002/admi.202400758 by Karlsruher Institut F., Wiley Online Library on [02/12/2024]. See the Terms and Conditions (https://onlinelibrary.wiley.com/terms-and-conditions) on Wiley Online Library for rules of use; OA articles are governed by the applicable Creative Commons License

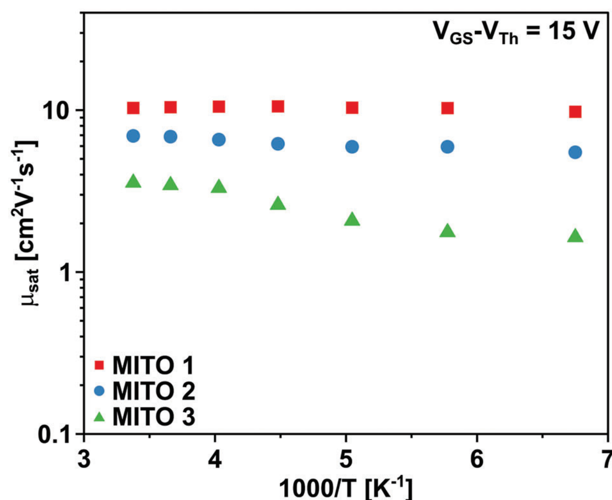

Figure 9. Arrhenius plot of the saturation mobility of the transistors MITO 1-3 (red, blue, green) as a function of the inverse temperature in the range of 295 – 148 K.

displays the Arrhenius plot of μ_{sat} between 295 and 148 K for the compositions MITO 1-3 of the transistors.

From the plot (Figure 9) it is evident that the transistor with the highest amount of magnesium oxide incorporation (MITO 3) shows a distinct temperature dependent behavior, which is expected for a TLC-dominated transport mechanism. Here, the mobility values remain nearly constant in the temperature range from 295 to 248 K at 3–3.4 cm^2 V^{-1} s^{-1} and then decreases significantly to 1.64 cm^2 V^{-1} s^{-1} at 148 K. In contrast, the mobility for MITO 1 remains at an almost constant value of ≈10.5 cm^2·V^{-1} s^{-1} in the range of 295–173 K, with only a slight decrease to 9.77 cm^2 V^{-1} s^{-1} at 148 K. These findings are indicative for PC being the prevalent electron conduction mechanism. As for MITO 2, the mobility shows a steady decrease with lowering temperatures, although not as drastic as for MITO 3, and therefore a trap-limited conduction is most likely to prevail (data for the whole temperature range can be found in Table S3, Supporting Information).

To assess the thermal and ambient stability of the heterostructure TFTs, the performance of the devices was evaluated after storage for 30 days at ambient conditions (air and humidity contact) under the exclusion of light. When measuring the devices without further annealing, the performance of the devices deteriorated to a significant extent (Figure S3, Supporting Information). The heterostack MITO 1 showed a strong shift toward conducting behavior, while MITO 2 and MITO 3 still displayed semiconducting behavior, although exhibiting a strong increase in I_{off} and a negative shift of V_{on}. After a repeated annealing step at 350 °C for 30 min, all devices exhibit semiconducting behavior and the performance parameters from before storage could partially be recovered. Interestingly enough, the mobility, threshold voltage and subthreshold swing of the devices MITO 2 and MITO 3 even exceed the initial values (Table S4, Supporting Information). Further experiments were conducted to elucidate the reason for the changing behavior. After storage for seven months in ambient conditions MITO 2 TFTs showed similar deterioration of the performance parameters and a subsequent annealing step was able to recover the performance to a certain extent, as described above. To verify the hypothesis that adsorbed water on the surface is responsible for the device degradation, the TFT substrate was immersed in water (HPLC Grade) for 30 min at room temperature and dried of with compressed air in order to restore the device. Afterwards the device performance showed a shift toward the behavior of the stored device, with a lower I_{on}/I_{off} ratio, a negative shift of V_{on} and an increased subthreshold swing (Figure S4 and Table S5, Supporting Information). The annealing and also the immersion in water was repeated two times, with a measurement following each step to get insight into the TFT performance under these harsh conditions and the need for encapsulation in humid environments in a real world application scenario. Each time the behavior changed as described above, however, recovering the electronic parameters following the annealing and deteriorating after the reaction with water. This leads to the conclusion that the intermittent deterioration of the devices after only a short period of time does originates from the adsorption of water molecules on the surface of the device, but can be reversed by thermal treatment. These findings are supported through reports by Hou et al. who found H_2O adsorption on the surface of MgO at room temperature, leading to a hydroxide surface layer, and the reversibility of the process at temperatures well above 100 °C.[88] Additionally, the dehydration of $Mg(OH)_2$ to MgO is reported to be occurring at temperatures ranging from 300 to 400 °C,[88–90] supporting the chosen annealing temperature of 350 °C. The hygroscopic nature of magnesium oxide has been reported in the literature and utilized in the form of a passivation layer for amorphous IGZO TFTs.[91] By employing a 20 nm thick layer of MgO on the back channel of the devices, the stability under positive bias stress and in humidity test could be improved, due to MgO reacting with water molecules from the air to form $Mg(OH)_2$.[91]

Further investigations on the performance stability of the heterostack TFT devices are conducted in the form of IV-measurements under illumination with light of different wavelength, ranging from the visible to the near ultraviolet region (2.0 – 3.7 eV). The devices are exposed to the specific wavelength for 10 min before and also during the IV-measurements and are referenced to a measurement performed under the exclusion of light. **Figure 10** shows the individual transfer curves of the three heterostacks MITO 1-3 with increasing energies of illumination.

For the three investigated heterostack TFT devices MITO 1-3, a clear difference between the measurements performed in the dark and the ones performed during illumination is evident. For MITO 1 and MITO 2 I_{off} is significantly increased, while a negative shift of V_{on} is visible for all three devices, when going from dark to illuminated. Comparing the transfer characteristics of the illumination experiments only, minor shifts are evident, especially for the heterostack MITO 3 with the highest amount of magnesium oxide incorporated into the film. For MITO 1 the increase of I_{off} amounts to 8.7·10^{-7} A, while for MITO 2 and MITO 3 the increase is merely 1.5·10^{-9} and 1.2·10^{-10} A, respectively, showing a favorable stability of all investigated heterostructures when exposed to light of a broad energy range (for performance parameters see **Table 4**). With MITO 3 exhibiting a band gap of 3.71 eV (Figure 6, Table 1), it is not surprising that no significant changes in the transfer characteristics and the respective performance parameters are apparent, as the highest energy of

 © 2024 The Author(s). Advanced Materials Interfaces published by Wiley-VCH GmbH

21967350, 0, Downloaded from https://onlinelibrary.wiley.com/doi/10.1002/admi.202400758 by Karlsruher Institut F., Wiley Online Library on [02/12/2024]. See the Terms and Conditions (https://onlinelibrary.wiley.com/terms-and-conditions) on Wiley Online Library for rules of use; OA articles are governed by the applicable Creative Commons License

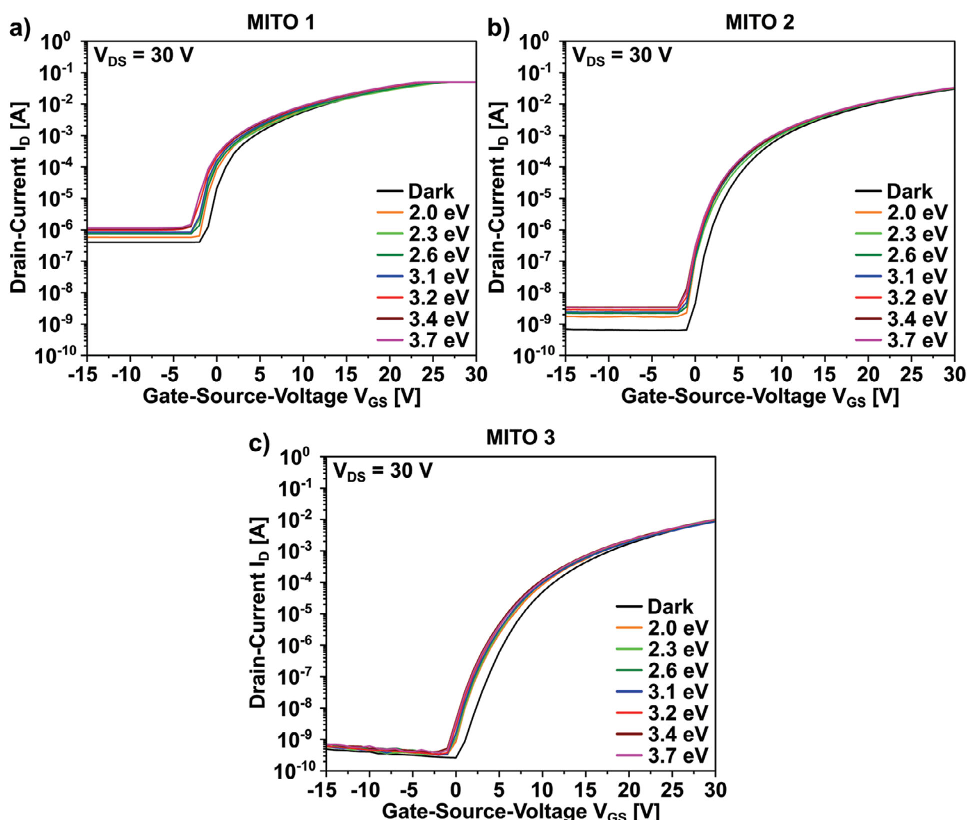

Figure 10. Transfer characteristics of the three TFT devices under illumination with energies ranging from 2.0 to 3.7 eV for the heterostacks MITO 1-3 a–c).

illumination exhibits the same value as the band gap. The band gaps of MITO 1 and MITO 2 with 3.57 and 3.62 eV, respectively, are slightly lower compared to the wavelength employed which might therefore show a stronger influence during the illumination experiments. Nevertheless, the influence on the TFT performance of light in the range of 2.0 to 3.7 eV is not as significant for the material combination MITO as it has been reported for other combinations, such as ITAO[92] or IZO[7] with considerable increases of I_{off} and negative shifts of V_{on}. These changes were assigned to the phenomenon of persistent photoconductivity (PPC), where charge carriers are generated in the semiconducting channel region by illumination.[93,94] These findings reveal that with the incorporation of only small amounts of magnesium oxide an increased stability under illumination with energies close to the band gap of the material can be achieved.

3. Conclusion

Thin-film heterostructures with a combination of insulating and conducting metal oxides have been fabricated via ALD. Indium-, tin-, and magnesium oxide were deposited at 200 °C by employing trimethylindium, tetrakis(dimethylamido)tin(IV), and bis(ethylcyclopentadienyl)-magnesium(II) as metal precursors and water as the oxidizing agent. With the layer-by-layer deposition process, the thickness of the individual oxides, and therefore the composition of the heterostack can be controlled accurately. The thin-films were found to exhibit a very disordered structure with correlations length of ≈10 Å, showing a high optical transparency of >95 % in the visible region, with a broadening of the optical band gap with increasing amounts of magnesium oxide. The influence of magnesium oxide on the performance parameters was studied by integrating the MITO heterostructures

Table 4. TFT performance parameters obtained under illumination with UV-light (3.7 eV) and in the dark for the heterostructures MITO 1-3 (V_{on} and I_{off} for all energies can be found in Table S6).

Composition In:Sn:MgO	Mobility μ_{sat} [cm^2 V^{-1} s^{-1}]		On-voltage V_{on} [V]		Threshold-voltage V_{th} [V]		Off-current I_{off} [A]		Current on/off ratio I_{on}/I_{off}		Subthreshold swing SS [mV dec^{-1}]	
	dark	3.7 eV	dark	3.7 eV	dark	3.7 eV	dark	3.7 eV	dark	3.7 eV	dark	3.7 eV
26:15:1 MITO 1	10.64	10.73	−2.0	−3.0	2.8	0.6	$4.0\cdot10^{-7}$	$1.5\cdot10^{-6}$	$1.2\cdot10^{5}$	$4.3\cdot10^{4}$	816	1059
26:15:2 MITO 2	6.45	6.82	−1.0	−2.0	7.2	6.6	$6.6\cdot10^{-10}$	$3.3\cdot10^{-9}$	$5.3\cdot10^{7}$	$1.0\cdot10^{7}$	644	699
26:15:3 MITO 3	3.06	2.81	0.0	−1.0	12.4	10.6	$2.6\cdot10^{-10}$	$4.5\cdot10^{-10}$	$3.4\cdot10^{7}$	$2.3\cdot10^{7}$	1211	1116

© 2024 The Author(s). Advanced Materials Interfaces published by Wiley-VCH GmbH

21967350, 0, Downloaded from https://onlinelibrary.wiley.com/doi/10.1002/admi.202400758 by Karlsruher Institut F., Wiley Online Library on [02/12/2024]. See the Terms and Conditions (https://onlinelibrary.wiley.com/terms-and-conditions) on Wiley Online Library for rules of use; OA articles are governed by the applicable Creative Commons License

into TFT devices. The optimized transistor (MITO 2) demonstrated a good overall device performance with an average saturation mobility (μ_{sat}) of 6.45 cm^2 V^{-1} s^{-1}, a current on/off (I_{on}/I_{off}) ratio of $5.3 \cdot 10^7$, on-voltage (V_{on}) of −1.0 V, and a subthreshold swing (SS) of 644 mV dec^{-1}. By incorporating even small amount of magnesium oxide, a strong influence on the TFT performance parameters was apparent, making it a suitable material for the reduction of oxygen vacancies, similar to Ga_2O_3, at the benefit of being an abundant, low-cost oxide. Additionally, the stability of the devices was investigated after storage under ambient conditions. The results showed a deterioration of the performance parameters after only a short period of time; however the electronic parameters could be recovered to a certain extent by an annealing step at 350 °C. This phenomenon was attributed to the adsorption and desorption of water molecules on the surface of the thin-films, pointing toward the need for encapsulation of these TFT devices under operating conditions. Furthermore, the behavior of the performance parameters under the influence of irradiation with light of different wavelengths was studied. By maintaining their semiconducting behavior with only minor changes of the performance parameters, especially an increase in I_{off} and a negative shift of V_{on}, the heterostructures MITO 1-3 demonstrated a favorable stability even under intense UV irradiation, owing to their wide optical band gap. The presented results outline a general strategy of employing a material combination of insulating and conducting oxides as semiconducting channel layer for TFTs. Considering the performance parameters being closely related to the composition of the thin-films, ALD is a superior fabrication technique, as the content of the individual oxides can be controlled on an atomic level.

4. Experimental Section

Methods: The deposition of the heterostacks was performed with an ALD Savannah S 100 system (Cambridge Ultratech) at a base pressure of 2.2 torr. During the process the ALD reactor was set to a temperature of 200 °C, while a constant flow of carrier gas (argon) of 20 sccm was ensured. Prior to deposition, the samples were kept inside the ALD reactor for 20 min at 200 °C under a constant argon flow. Precursors employed for the metal oxides were trimethylindium (TMI, 99.999 %, AkzoNobel), tetrakis(dimethylamido)tin (TDMASn),[95] and bis(ethylcyclopentadienyl)magnesium, $(EtCp)_2Mg$,[96] for indium oxide, tin oxide, and magnesium oxide, respectively. Water (HPLC grade, Sigma–Aldrich) was used as oxidizing agent. TMI and water were kept at room temperature, while TDMASn and $(EtCp)_2Mg$ were heated to 60 and 90 °C, respectively. As carrier gas Argon (99.9999 %, AlphaGaz) was used and set to a constant flow of 20 sccm during the deposition process. The parameters for the deposition of indium oxide were: TMI pulse 1 s, exposition 10 s, argon purge 30 s, H_2O pulse 0.1 s, exposition 1.5 s, argon purge 20 s. For tin oxide the sequence was: TDMASn pulse 0.5 s, exposition 1.5 s, argon purge 30 s, H_2O pulse 0.015 s, exposition 1.5 s, argon purge 30 s. For magnesium oxide the following parameters were used: $(EtCp)_2Mg$ pulse 1 s, exposition 10 s, argon purge 30 s, H_2O pulse 0.015 s, exposition 1.5 s, argon purge 20 s. For the compositional modulation the numbers of indium oxide and tin oxide cycles were kept constant at 26 and 15, respectively, while the number of magnesium oxide cycles were varied between one and three. The overall thickness of the film was modulated by the repetition of an ALD supercycle with a constant composition: Here, eight iterations were found to produce the optimal film thickness.

Material Characterization: Film thicknesses were obtained by ellipsometry using a spectroscopic ellipsometer M2000 (J.A. Woollam) in a spectral range of 370–1690 nm and an angular range of 45–85°. Samples used were coated Si/SiO_2-Substrates, annealed at 350 °C for 40 min. For UV–vis characterization coated and annealed (40 min @ 350 °C) quartz substrates were measured with an Evolution 600 spectrometer (Thermo Scientific) in a wavelength range from 190–900 nm. For high resolution transmission electron microscopy (HRTEM) investigations TFT-substrates with the deposited ALD heterostacks were used as samples. These were annealed at 350 °C for 40 min and electrically characterized beforehand. HRTEM was performed with a FEI Tecnai G2 F20 with an operating voltage of 200 keV.[97] Samples for focused ion beam (FIB) were prepared using a gallium-focused ion beam (FEI Helios NanoLab 460F1 FIB-SEM) and a subsequent coating with a platinum layer.[98] X-ray photoelectron spectroscopy (XPS) measurements were performed using a K-Alpha+ XPS spectrometer (ThermoFisher Scientific, East Grinstead, UK). Data acquisition and processing using the Thermo Avantage software is described elsewhere.[99] All samples were analyzed using a microfocused, monochromated Al Kα X-ray source (400 µm spot size). The K-Alpha+ charge compensation system was employed during analysis, using electrons of 8 eV energy, and low-energy argon ions to prevent any localized charge build-up. The spectra were fitted with one or more Voigt profiles (BE uncertainty: ±0.2 eV) and Scofield sensitivity factors were applied for quantification.[100] All spectra were referenced to the C 1s peak (C—C, C—H) at 285.0 eV binding energy controlled by means of the well-known photoelectron peaks of metallic Cu, Ag, and Au, respectively. Coated and annealed (40 minutes @ 350 °C) Si/SiO_2 substrates were used as samples. Grazing incidence X-ray total scattering (GI-XTS) measurements were conducted at beamline P21.1 at the storage ring PETRA III, DESY, Germany. The X-ray beam of 101.6 keV was focused by means of compound refractive lenses to a size of ≈2 × 150 µm^2 (vertical by horizontal).[101] A PerkinElmer XRD1621 amorphous silicon flat panel detector was mounted at a sample distance of ≈400 mm. Data was collected through single exposure at an incidence angle of 0.02° with an optimized signal-to-background ratio. For the azimuthal integration of the 2D diffraction patterns pyFAI[102] was used, while the conversion into the PDF was carried out using PDFgetX3[103] implemented into the xPDFsuite package.[104] Quartz slides with a size of 10 × 10 mm^2 and a thickness of 0.12 mm were used as substrates. Thin-films with a composition of 26:15:2 (MITO) and 26:15 (ITO) were deposited in 16 supercycles, with film thicknesses of 22.0 and 14.4 nm, respectively. After the deposition the samples were annealed on a hot ceramic plate for 60 minutes at 350 °C.

Electrical Characterization: Commercial substrates (Fraunhofer IMPS, Dresden) with prefabricated source-drain electrodes in a bottom-gate-bottom-contact (BGBC) device geometry were used for TFT characterization. The substrates comprise of highly n-doped silicon with a 90 nm silicon dioxide layer on top. Source-drain electrodes exhibit an interdigital structure with a channel length of L = 20 µm and width of W = 10 mm (W/L = 500), consisting of 40 nm gold with a 10 nm thick indium tin oxide (ITO) adhesion layer below.[105] All used substrates (TFT, Si/SiO_2, quartz) were cleaned via ultrasonication using acetone, water, and isopropanol (HPLC grades, Carl Roth GmbH & Co. KG) for 10 min, subsequently. Directly before deposition the substrates were treated with UV light (UV Ozone Cleaner UVC-1014, NanoBioAnalytics) for 10 min, at a wavelength of 254 nm employing an optical power of 4 W.[106] Characterization of the TFTs was performed under exclusion of white light, in an inert environment inside a glovebox (O_2 < 0.5 ppm, H_2O < 0.5 ppm), employing a B1500A Semiconductor Device Analyzer (Agilent Technologies). Prior to the electrical measurements, all deposited thin-films were annealed in air at 350 °C for a duration of 40 min. The characterization under illumination was done using individual light emitting diodes (Roitner Laser Technik GmbH) of different wavelength ranging from the visible to the UV region (605, 532, 470, 405, 389, 360, and 340 nm). Measurements at low temperatures were performed by means of cooling with liquid nitrogen, with temperatures ranging from room temperature to 148 K. The temperature was reduced in steps of 25 K, maintaining the samples at the set temperature for 30 min before the measurement. From a linear fit of the square root of the source-drain current (I_{DS}), as function of the gate-source voltage (V_{GS}), the charge carrier mobility (μ_{sat}) and threshold voltage (V_{th}) were extracted. For each

© 2024 The Author(s). Advanced Materials Interfaces published by Wiley-VCH GmbH

composition 16 transistors were measured, fabricated in four independent ALD processes.

For Hall-measurements the thin-films were deposited on quartz substrates with 80 nm Pt/Pd contacts on all four corners and annealed at 350 °C for 30 min. Measurements were performed at room temperature in the form of 4-point measurements using the Van der Pauw geometry with a magnetic field of 1.3 T and currents ranging from $2{\cdot}10^{-1} - 5{\cdot}10^{-3}$ mA. A LakeShore EM4-HVA magnet with 52 mm pole caps with a LakeShore Model 643 Electromagnet power supply was used. The magnet and power supply are water cooled. The magnetic field is controlled by a LakeShore 475 DSP Gaussmeter and the currents for the measurements are provides by a Keithley 2635A System SourceMeter. Additionally, a Keithley 2700 Multimeter with installed 7709 Switching Card was used.

Supporting Information

Supporting Information is available from the Wiley Online Library or from the author.

Acknowledgements

TEM sample preparation and measurements were done at the Ernst-Ruska Center (ERC) Jülich under contract ERC-TUDa. The authors thank Jörg Engstler (TUDa) for experimental assistance. The authors were grateful to Alexander Creutz for Hall measurements (group of Andreas Klein, Dep. of Materials Science at TUDa). Ann-Christin Dippel (DESY) acknowledges the use of beamline equipment funded through BMBF grant 05K22RF. The authors cordially thank the reviewers for valuable comments during the refereing process.

Conflict of Interest

The authors declare no conflict of interest.

Data Availability Statement

The data that support the findings of this study are available from the corresponding author upon reasonable request.

Keywords

atomic layer deposition, doped indium tin oxide, magnesium oxide, thin-film transistors

Received: September 19, 2024
Revised: October 24, 2024
Published online:

[1] J. Lee, D. S. Chung, *J. Mater. Chem. C* **2023**, *11*, 5241.
[2] Y. Zeng, H. Ning, Z. Zheng, H. Zhang, Z. Fang, R. Yao, M. Xu, L. Wang, L. Lan, J. Peng, X. Lu, *Appl. Phys. Lett.* **2017**, *110*, 153503.
[3] W. Xu, H. Li, J.-B. Xu, L. Wang, *ACS Appl. Mater. Interfaces* **2018**, *10*, 25878.
[4] H. Faber, S. Das, Y.-H. Lin, N. Pliatsikas, K. Zhao, T. Kehagias, G. Dimitrakopulos, A. Amassian, P. A. Patsalas, T. D. Anthopoulos, *Sci. Adv.* **2017**, *3*, 1602640.
[5] K. Tetzner, I. Isakov, A. Regoutz, D. J. Payne, T. D. Anthopoulos, *J. Mater. Chem. C* **2017**, *5*, 59.
[6] S. Sanctis, J. Krausmann, C. Guhl, J. J. Schneider, *J. Mater. Chem. C* **2018**, *6*, 464.
[7] J. Krausmann, S. Sanctis, J. Engstler, M. Luysberg, M. Bruns, J. J. Schneider, *ACS Appl. Mater. Interfaces* **2018**, *10*, 20661.
[8] S. Cho, J.-H. Yang, J. G. Oh, S.-H. Cho, C.-S. Hwang, J. Jang, S. Nam, *J. Mater. Chem. C* **2017**, *5*, 6521.
[9] W.-C. Jhang, P.-H. Chen, C.-C. Hsu, U. Nanda, *J. Mater. Chem. C* **2023**, *11*, 5750.
[10] G.-B. Kim, N. On, T. Kim, C. H. Choi, J. S. Hur, J. H. Lim, J. K. Jeong, *Small Methods* **2023**, *7*, 2201522.
[11] R. N. Bukke, N. N. Mude, J. K. Saha, J. Jang, *Adv. Mater. Interfaces* **2019**, *6*, 1900277.
[12] K. Nomura, T. Kamiya, M. Hirano, H. Hosono, *Appl. Phys. Lett.* **2009**, *95*, 13502.
[13] T. Kamiya, K. Nomura, H. Hosono, *Sci. Technol. Adv. Mater.* **2010**, *11*, 044305.
[14] J. K. Jeong, J. H. Jeong, H. W. Yang, J.-S. Park, Y.-G. Mo, H. D. Kim, *Appl. Phys. Lett.* **2007**, *91*, 113505.
[15] A. Olziersky, P. Barquinha, A. Vilà, C. Magaña, E. Fortunato, J. R. Morante, R. Martins, *Mater. Chem. Phys.* **2011**, *131*, 512.
[16] B. K. Yap, Z. Zhang, G. S. H. Thien, K.-Y. Chan, C. Y. Tan, *Appl. Surf. Sci. Adv.* **2023**, *16*, 100423.
[17] R. L. Weiher, *J. Appl. Phys.* **1962**, *33*, 2834.
[18] H. B. Kim, H. S. Lee, *Thin Solid Films* **2014**, *550*, 504.
[19] B. Cheng, J. M. Russell, W. Shi, L. Zhang, E. T. Samulski, *J. Am. Chem. Soc.* **2004**, *126*, 5972.
[20] R. Bel Hadj Tahar, T. Ban, Y. Ohya, Y. Takahashi, *J. Appl. Phys.* **1998**, *83*, 2631.
[21] Y. Shao, X. Xiao, L. Wang, Y. Liu, S. Zhang, *Adv. Funct. Mater.* **2014**, *24*, 4170.
[22] J.-I. Kim, K. H. Ji, M. Jang, H. Yang, R. Choi, J. K. Jeong, *ACS Appl. Mater. Interfaces* **2011**, *3*, 2522.
[23] D.-H. Cho, S. Yang, C. Byun, J. Shin, M. K. Ryu, S.-H. K. Park, C.-S. Hwang, S. M. Chung, W.-S. Cheong, S. M. Yoon, H.-Y. Chu, *Appl. Phys. Lett.* **2008**, *93*, 142111.
[24] Y. S. Rim, D. L. Kim, W. H. Jeong, H. J. Kim, *Appl. Phys. Lett.* **2010**, *97*, 233502.
[25] Y. Jeong, K. Song, T. Jun, S. Jeong, J. Moon, *Thin Solid Films* **2011**, *519*, 6164.
[26] S. Parthiban, J.-Y. Kwon, *J. Mater. Res.* **2014**, *29*, 1585.
[27] J. S. Wrench, I. F. Brunell, P. R. Chalker, J. D. Jin, A. Shaw, I. Z. Mitrovic, S. Hall, *Appl. Phys. Lett.* **2014**, *105*, 202109.
[28] C.-Y. Zhao, J. Li, D.-Y. Zhong, C.-X. Huang, J.-H. Zhang, X.-F. Li, X.-Y. Jiang, Z.-L. Zhang, *IEEE Trans. Electron. Devices* **2017**, *64*, 2216.
[29] H. Zhang, Y. Meng, L. Song, L. Luo, Y. Qin, N. Han, Z. Yang, L. Liu, J. C. Ho, F. Wang, *Nano. Res.* **2018**, *11*, 1227.
[30] J. K. Yao, F. Ye, P. Fan, *Opt. Mater. Express, OME* **2018**, *8*, 3438.
[31] W. H. Jeong, G. H. Kim, D. L. Kim, H. S. Shin, H. J. Kim, M.-K. Ryu, K.-B. Park, J.-B. Seon, S.-Y. Lee, *Thin Solid Films* **2011**, *519*, 5740.
[32] C.-J. Kim, S. Kim, J.-H. Lee, J.-S. Park, S. Kim, J. Park, E. Lee, J. Lee, Y. Park, J. H. Kim, S. T. Shin, U.-I. Chung, *Appl. Phys. Lett.* **2009**, *95*, 252103.
[33] M. I. Büschges, V. Trouillet, J. J. Schneider, *J. Mater. Chem. C* **2022**, *10*, 5447.
[34] D.-H. Kim, D.-H. Son, S.-J. Sung, J.-H. Kim, J.-K. Kang, *Mol. Cryst. Liq. Cryst.* **2012**, *564*, 130.
[35] J.-S. Park, K. Kim, Y.-G. Park, Y.-G. Mo, H. D. Kim, J. K. Jeong, *Adv. Mater.* **2009**, *21*, 329.
[36] J. Sheng, J.-H. Lee, W.-H. Choi, T. Hong, M. Kim, J.-S. Park, *J. Vac. Sci. Technol. A* **2018**, *36*, 60801.
[37] A. J. M. Mackus, J. R. Schneider, C. MacIsaac, J. G. Baker, S. F. Bent, *Chem. Mater.* **2019**, *31*, 1142.

© 2024 The Author(s). Advanced Materials Interfaces published by Wiley-VCH GmbH

21967350, 0, Downloaded from https://onlinelibrary.wiley.com/doi/10.1002/admi.202400758 by Karlsruher Institut F., Wiley Online Library on [02/12/2024]. See the Terms and Conditions (https://onlinelibrary.wiley.com/terms-and-conditions) on Wiley Online Library for rules of use; OA articles are governed by the applicable Creative Commons License

[38] S. Yasmeen, S. W. Ryu, S.-H. Lee, H.-B.-R. Lee, *Adv. Mater. Technol.* **2023**, *8*, 2200876.
[39] H.-M. Kim, D.-G. Kim, Y.-S. Kim, M. Kim, J.-S. Park, *Int. J. Extrem. Manuf.* **2023**, *5*, 012006.
[40] K. Nomura, H. Ohta, A. Takagi, T. Kamiya, M. Hirano, H. Hosono, *Nature* **2004**, *432*, 488.
[41] J. Sheng, T. Hong, H.-M. Lee, K. Kim, M. Sasase, J. Kim, H. Hosono, J.-S. Park, *ACS Appl. Mater. Interfaces* **2019**, *11*, 40300.
[42] V. Miikkulainen, M. Leskelä, M. Ritala, R. L. Puurunen, *J. Appl. Phys.* **2013**, *113*, 21301.
[43] X. Meng, X.-Q. Yang, X. Sun, *Adv. Mater.* **2012**, *24*, 3589.
[44] A. F. Palmstrom, P. K. Santra, S. F. Bent, *NanoscaleNanoscale* **2015**, *7*, 12266.
[45] B. J. O'Neill, D. H. K. Jackson, J. Lee, C. Canlas, P. C. Stair, C. L. Marshall, J. W. Elam, T. F. Kuech, J. A. Dumesic, G. W. Huber, *ACS Catal.* **2015**, *5*, 1804.
[46] M. R. Laskar, D. H. K. Jackson, S. Xu, R. J. Hamers, D. Morgan, T. F. Kuech, *ACS Appl. Mater. Interfaces* **2017**, *9*, 11231.
[47] R. Huang, A. H. Kitai, *J. Electron. Mater.* **1993**, *22*, 215.
[48] W. Zachariasen, *Nor. J. Geol.* **1927**, *9*, 310.
[49] N. Nadaud, N. Lequeux, M. Nanot, J. Jové, T. Roisnel, *J. Solid State Chem.* **1998**, *135*, 140.
[50] N. Nadaud, M. Nanot, J. Jové, T. Roisnel, *KEM* **1997**, *132*, 1373.
[51] G. B. González, J. S. Okasinski, T. O. Mason, T. Buslaps, V. Honkimäki, *J. Appl. Phys.* **2008**, *104*, 43520.
[52] W. H. Baur, *Acta Cryst.* **1956**, *9*, 515.
[53] E. Broch, *Z. Phys. Chem. (N F)* **1927**, *127U*, 446.
[54] J. Socratous, K. K. Banger, Y. Vaynzof, A. Sadhanala, A. D. Brown, A. Sepe, U. Steiner, H. Sirringhaus, *Adv. Funct. Mater.* **2015**, *25*, 1873.
[55] N. Koslowski, V. Trouillet, J. J. Schneider, *J. Mater. Chem. C* **2020**, *8*, 8521.
[56] J. Stoch, J. Gablankowska-Kukucz, *Surf. Interface. Anal.* **1991**, *17*, 165.
[57] J. C. Hackley, T. Gougousi, *Thin Solid Films* **2009**, *517*, 6576.
[58] G. Chistiakova, B. Macco, L. Korte, *IEEE J. Photovolt.* **2020**, *10*, 398.
[59] K. K. Banger, Y. Yamashita, K. Mori, R. L. Peterson, T. Leedham, J. Rickard, H. Sirringhaus, *Nat. Mater.* **2011**, *10*, 45.
[60] S.-J. Seo, Y. H. Hwang, B.-S. Bae, *Electrochem. Solid-State Lett.* **2010**, *13*, H357.
[61] C. Donley, D. Dunphy, D. Paine, C. Carter, K. Nebesny, P. Lee, D. Alloway, N. R. Armstrong, *Langmuir* **2002**, *18*, 450.
[62] Y. Zhao, L. Duan, G. Dong, D. Zhang, J. Qiao, L. Wang, Y. Qiu, *Langmuir* **2013**, *29*, 151.
[63] H. Idriss, *Surf. Sci.* **2021**, *712*, 121894.
[64] M. Santamaria, F. Di Quarto, S. Zanna, P. Marcus, *Electrochim. Acta.* **2007**, *53*, 1314.
[65] S. Feliu, M. L. Pérez-Revenga, *Metall. Mater. Trans. A Phys. Metall. Mater. Sci.* **2004**, *35*, 2039.
[66] S. Feliu Jr, M. C. Merino, R. Arrabal, A. E. Coy, E. Matykina, *Surf. Interface. Anal.* **2009**, *41*, 143.
[67] V. Fournier, P. Marcus, I. Olefjord, *Surf. Interface. Anal.* **2002**, *34*, 494.
[68] F. Borgatti, J. A. Berger, D. Céolin, J. S. Zhou, J. J. Kas, M. Guzzo, C. F. McConville, F. Offi, G. Panaccione, A. Regoutz, D. J. Payne, J.-P. Rueff, O. Bierwagen, M. E. White, J. S. Speck, M. Gatti, R. G. Egdell, *Phys. Rev. B* **2018**, *97*, 155102.
[69] S. D. Ponja, B. A. D. Williamson, S. Sathasivam, D. O. Scanlon, I. P. Parkin, C. J. Carmalt, *J. Mater. Chem. C* **2018**, *6*, 7257.
[70] Z. M. Detweiler, S. M. Wulfsberg, M. G. Frith, A. B. Bocarsly, S. L. Bernasek, *Surf. Sci.* **2016**, *648*, 188.
[71] F. Khairallah, A. Glisenti, *Surf. Sci. Spectra* **2006**, *13*, 58.
[72] V. Kumar, N. Singh, R. M. Mehra, A. Kapoor, L. P. Purohit, H. C. Swart, *Thin Solid Films* **2013**, *539*, 161.
[73] S. Vangelista, R. Mantovan, A. Lamperti, G. Tallarida, B. Kutrzeba-Kotowska, S. Spiga, M. Fanciulli, *J. Phys. D: Appl. Phys.* **2013**, *46*, 485304.
[74] H. Wang, K. Fu, *J. Vac. Sci. Technol. A* **2013**, *31*, 06F101.
[75] B. Yan, S. Liu, Y. Yang, Y. Heng, *Appl. Surf. Sci.* **2016**, *371*, 118.
[76] X. Bi, J. Yao, S. Zhang, in *2014 IEEE International Conference on Electron Devices and Solid-State Circuits*, IEEE, Piscataway, NJ **2014**.
[77] H. Köstlin, R. Jost, W. Lems, *Phys. Status Solidi A* **1975**, *29*, 87.
[78] L.-C. Yang, D.-R. Jung, F.-R. Po, C.-H. Hus, J.-S. Fang, *Coatings* **2020**, *10*, 708.
[79] R. Soto, S. Mergui, P. Schmidt, *Thin Solid Films* **1997**, *308*, 611.
[80] Y.-R. Luo, *Comprehensive Handbook of Chemical Bond Energies*, CRC Press Taylor & Francis, Boca Raton, London, New York, **2007**.
[81] Y.-R. Luo, J. A. Kerr, *Handbook of Bond Dissociation Energies in Organic Compounds*, CRC Taylor & Francis, Boca Raton, London, New York, **2012**, *89*, 65.
[82] Y. Kwon, Y. Li, Y. W. Heo, M. Jones, P. H. Holloway, D. P. Norton, Z. V. Park, S. Li, *Appl. Phys. Lett.* **2004**, *84*, 2685.
[83] T. Kamiya, K. Nomura, H. Hosono, *J. Display Technol.* **2009**, *5*, 273.
[84] S. Lee, K. Ghaffarzadeh, A. Nathan, J. Robertson, S. Jeon, C. Kim, I.-H. Song, U.-I. Chung, *Appl. Phys. Lett.* **2011**, *98*, 203508.
[85] T. Kamiya, H. Hosono, *NPG Asia Mater* **2010**, *2*, 15.
[86] J. Kim, T. Sekiya, N. Miyokawa, N. Watanabe, K. Kimoto, K. Ide, Y. Toda, S. Ueda, N. Ohashi, H. Hiramatsu, H. Hosono, T. Kamiya, *NPG Asia Mater* **2017**, *9*, e359.
[87] J. Sheng, E. J. Park, B. Shong, J.-S. Park, *ACS Appl. Mater. Interfaces* **2017**, *9*, 23934.
[88] Q. Hou, J. Li, L. Xudong, Z. Xie, D. An, *J. Asia Ceram. Soc.* **2022**, *10*, 130.
[89] M. S. Mel'gunov, V. B. Fenelonov, E. A. Mel'gunova, A. F. Bedilo, K. J. Klabunde, *J. Phys. Chem. B* **2003**, *107*, 2427.
[90] M. Kitagawa, S. Misu, J. Ichikawa, H. Matsuhashi, *Res. Chem. Intermed.* **2015**, *41*, 9463.
[91] D. Y. Yoo, E. Chong, D. H. Kim, B. K. Ju, S. Y. Lee, *Thin Solid Films* **2012**, *520*, 3783.
[92] M. I. Büschges, R. C. Hoffmann, A. Regoutz, C. Schlueter, J. J. Schneider, *Chem. - Eur. J.* **2021**, *27*, 9791.
[93] K. Ide, K. Nomura, H. Hosono, T. Kamiya, *Phys. Status Solidi A* **2019**, *216*, 1800372.
[94] A. Sumanth, K. Lakshmi Ganapathi, M. S. Ramachandra Rao, T. Dixit, *J. Phys. D: Appl. Phys.* **2022**, *55*, 393001.
[95] K. Jones, M. F. Lappert, *J. Organomet. Chem.* **1965**, *3*, 295.
[96] A. N. Nesmeyanov, K. N. Anisimov, Z. P. Valueva, *Bull. Acad. Sci. USSR* **1961**, *10*, 1659.
[97] M. Luysberg, M. Heggen, K. Tillmann, *JLSRF* **2016**, *2*, A77.
[98] M. Kruth, D. Meertens, K. Tillmann, *JLSRF* **2016**, *2*, A59.
[99] K. L. Parry, A. G. Shard, R. D. Short, R. G. White, J. D. Whittle, A. Wright, *Surf. Interface. Anal.* **2006**, *38*, 1497.
[100] J. H. Scofield, *Phenom. J.* **1976**, *8*, 129.
[101] F. Bertram, O. Gutowski, J. Patommel, C. Schroer, U. Ruett, *AIP Conf. Proc* **2016**, *1741*, 40003.
[102] J. Kieffer, J. P. Wright, *Powder Diffr.* **2013**, *28*, S339.
[103] P. Juhás, T. Davis, C. L. Farrow, S. J. L. Billinge, *J. Appl. Cryst.* **2013**, *46*, 560.
[104] X. Yang, P. Juhas, C. L. Farrow, S. J. L. Billinge, *arXiv* **2014**, 14023163.
[105] Fraunhofer I. P. M. S., End-of-Line Standard Substrates for the Characterization of Organic Semiconductor Materials: OFET-Structures on Silicon with Au Source/Drain and 90 nm SiO2 Gate-Insulator Generation 4, https://www.ipms.fraunhofer.de/content/dam/ipms/common/documents/end-of-line-substrates_stand_E-Mail.pdf.
[106] NanoBioAnalytics, UV-Ozon-Reiniger UVC-1014, http://www.nanobioanalytics.com/UVC-1014.php.

© 2024 The Author(s). Advanced Materials Interfaces published by Wiley-VCH GmbH

21967350, 0, Downloaded from https://onlinelibrary.wiley.com/doi/10.1002/admi.202400758 by Karlsruher Institut F., Wiley Online Library on [02/12/2024]. See the Terms and Conditions (https://onlinelibrary.wiley.com/terms-and-conditions) on Wiley Online Library for rules of use; OA articles are governed by the applicable Creative Commons License